J. Fluid Mech. (2000), *vol.* 416, *pp.* 1–28. Printed in the United Kingdom

Vortex formation in front of a piston moving through a cylinder

By J. J. ALLEN AND M. S. CHONG

The University of Melbourne, Department of Mechanical and Manufacturing Engineering, Parkville, Victoria 3052, Australia

(Received 13 June 1997 and in revised form 12 January 2000)

This paper contains the details of an experimental study of the vortex formed in front of a piston as it moves through a cylinder. The mechanism for the formation of this vortex is the removal of the boundary layer forming on the cylinder wall in front of the advancing piston. The trajectory of the vortex core and the vorticity distribution on the developing vortex have been measured for a range of piston velocities. Velocity field measurements indicate that the vortex is essentially an inviscid structure at the Reynolds numbers considered, with viscous effects limited to the immediate corner region. Inviscid flow is defined in this paper as being a region of the flow where inertial forces are significantly larger than viscous forces. Flow visualization and vorticity measurements show that the vortex is composed mainly of material from the boundary layer forming over the cylinder wall. The characteristic dimension of the vortex appears to scale in a self-similar fashion, while it is small in relation to the apparatus length scale. This scaling rate of $t^{0.85+0.7m}$, where the piston speed is described as a power law At^m, is somewhat faster than the $t^{3/4}$ scaling predicted by Tabaczynski *et al.* (1970) and considerably faster than a viscous scaling rate of $t^{1/2}$. The reason for the structure scaling more rapidly than predicted is the self-induced effect of the secondary vorticity that is generated on the piston face. The vorticity distribution shows a distinct spiral structure that is smoothed by the action of viscosity. The strength of the separated vortex also appears to scale in a self-similar fashion as t^{2m+1}. This rate is the same as suggested from a simple model of the flow that approximates the vorticity being ejected from the corner as being equivalent to the flux of vorticity over a flat plate started from rest. However, the strength of the vorticity on the separated structure is 25% of that suggested by this model, sometimes referred to as the 'slug' model. Results show that significant secondary vorticity is generated on the piston face, forming in response to the separating primary vortex. This secondary vorticity grows at the same rate as the primary vorticity and is wrapped around the outside of the primary structure and causes it to advect away from the piston surface.

1. Introduction

Vortex rings and separated flows have been the topic of a range of experimental and analytic studies. However, quantitative information is limited regarding the nature of the vortex formed in the region close to the junction of two perpendicular surfaces moving relative to each other. Figure 1 shows a diagram of a segment of this class of vortex forming in front of a circular piston.

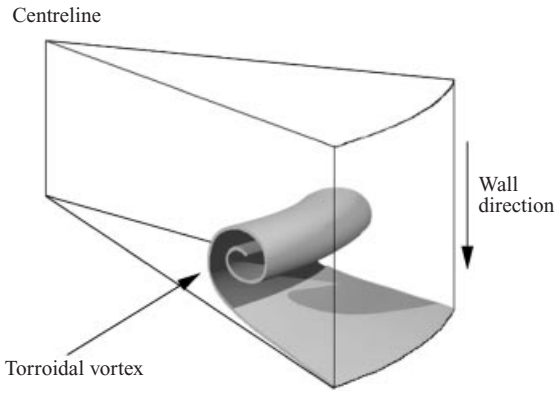

FIGURE 1. Schematic diagram of the vortex development in front of a circular piston.

The aim of this study is to classify the vortex, identify the possible factors affecting its formation and growth and develop scaling laws for its important features. To accomplish this a series of experiments was conducted to measure the spatial development of the vortex and the distribution of vorticity in front of the piston for a varying range of experimental conditions.

The experiments of Hughes & Gerrard (1971) showed that the boundary layer material, scraped off the stationary surface by the advancing piston, separated from the piston face and rolled into a vortical structure. This vortex was composed of the separated boundary layer and entrained material from the surrounding quiescent fluid. The Reynolds number ($Re_{apparatus} = U_w D/\nu$ where D is the piston diameter and U_w is the piston speed) was greater than 400 for roll-up to occur. $Re_{apparatus}$ was constant for the duration of an experiment.

Tabaczynski, Hoult & Keck (1970) and Daneshyar, Fuller & Deckker (1973) conducted flow visualization experiments to examine the transient development of this class of vortex. Tabaczynski *et al.* (1970) postulated that the cross-sectional area of the vortex was a function of the piston speed and the distance the piston had moved from rest. The area of the vortex was defined as the area of the separated primary vortex and in experiments the area was marked by a dye streakline. By assuming that the size of the vortex was small in relation to the apparatus length scale (piston diameter) an analytic expression was developed for the cross-sectional area of the laminar vortex by assuming that the area of the boundary layer forming on the cylinder wall was proportional to the area of the vortex. The analysis suggested that the characteristic dimension the vortex should scale as $t^{3/4}$. Although it was a hard to determine from the flow visualization pictures, Tabaczynski *et al.* (1970) stated that for Reynolds numbers $Re_{vortex} = U_w L_w/\nu$, where L_w is the distance the piston has moved from rest, greater than 15 000 the vortex became turbulent. Re_{vortex} is a Reynolds number that increases during vortex development. For a turbulent vortex it was suggested that the rate of change of its cross-sectional area is proportional to the product of the perimeter of the vortex and the velocity of the piston. This resulted in the prediction that the size of the vortex should scale linearly with time when turbulent. Reasonable agreement was found between experiments and predictions. However, the data were scattered due to a 25% error in the estimation of the area of the vortex from the flow visualization photographs and a 10% error in the estimation of the location and velocity of the piston. The experimental results suggested that 85% of the vortical structure is the material from the separated boundary layer. The

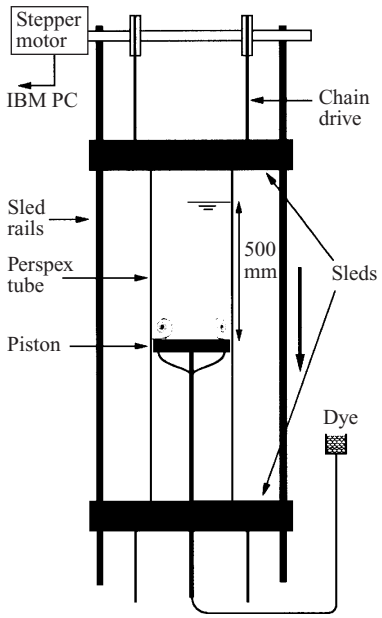

FIGURE 2. Axisymmetric vortex generator.

remaining 15% is the result of inviscid entrainment. The experiments of Daneshyar *et al.* (1973) involved moving a rectangular piston with a sinusoidal velocity characteristic and using dye for flow visualization. As in the study of Tabaczynski *et al.* (1970), in order to develop an analytic expression for the vortex scaling, it was assumed that the area of the boundary layer forming over the duct wall is proportional to the cross-sectional area of the vortex. The experiments agreed reasonably well with the analytic predictions until turbulent transition.

Similar vortices occur in an engine cylinder when the piston moves through the exhaust and compression strokes. Researchers in the automotive field, e.g. Obokata & Okajima (1992), Namazian *et al.* (1981), and Ishikawa & Daily (1978), observed vortex formation at the head of a piston using smoke visualization and schlieren photography. However, little quantitative information was collected about the vortex development due to the poor quality of the experimental results.

2. Apparatus and experimental techniques

In order to examine the vortex at the head of a circular piston an experimental apparatus was designed such that the piston was fixed while the outside cylinder was moved relative to the piston. The benefit of such an apparatus is that it reduced the system inertia and enabled the camera to remain fixed. An overall schematic of the experimental apparatus used to generate an axisymmetric vortex in front of a circular piston is shown in figure 2.

The experiments were conducted in cylinders of two different internal diameters, 138 and 170 mm. These large diameters were chosen in order to maximize the resolution of the vortical structure being formed at the cylinder wall/piston junction and to reduce the effects of the experimental length scale, i.e. the cylinder diameter, on the vortex development. The pistons were fitted with rubber gaskets to stop leakage. A square viewing tank was fitted around the outside of the Perspex tube to minimize parallax

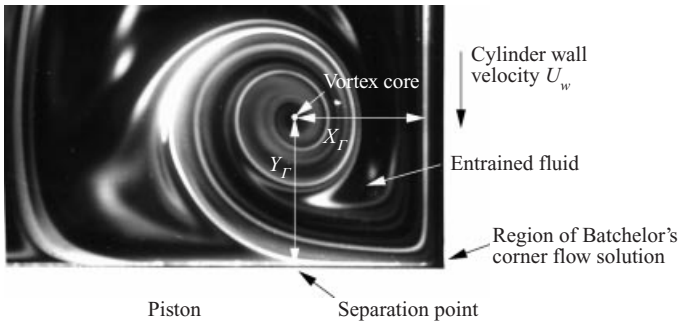

FIGURE 3. Flow visualization results from the current study with the features of the vortex labelled.

error associated with recording images of the vortical structure. The vertical distance between the piston and the free surface in the cylinder was 500 mm. A computer-controlled stepper motor enabled the cylinder wall to be driven with accurate and repeatable velocity characteristics of the form $U_w = At^m$, where U_w is the cylinder wall speed. A stepper motor drove a sled to which the cylinder was attached. Accurate determination of the start of motion and hence the vortex roll-up was achieved with a photo-diode that detected the start of sled motion. This photo diode in turn was linked to an LED which was turned off when motion started and hence enabled the time of the start of the cylinder motion to be recorded to within 1/25th of a second from a video of the vortex roll-up. The wall speed was calibrated by recording the motion of the cylinder and then curve fitting $L_w = At^{m+1}/(m+1)$ to the displacement data to determine A and m. Both the flow visualization experiments and particle tracking experiments involved taking an illuminated cross-section through the centreline of the piston. This was accomplished with an argon-ion laser and a cylindrical and spherical lens system to generate a 1 mm thick illumination sheet. The flow visualization experiments used fluorescent dye to mark the developing vortex. The vortex was made visible by leaking dye into the working section via the piston through a 1 mm diameter hole close to the piston/cylinder junction. Careful injection of dye was required so as not to disturb the structure of the developing vortex. The dye was introduced at this location because this is where the boundary layer is removed from the cylinder wall and close to where it subsequently separates from the piston. The illumination sheet was configured to pass through the cylinder centreline and the injector hole. Once the dye had begun to leak into the cavity the cylinder was set in motion and the developing vortex recorded on video tape. Images from the video tape, with time codes, were subsequently digitized with a frame grabber and enhanced for experimental evaluation of the location of the vortex core. An example of the experimental results using fluorescent dye with the important features of the vortex labelled, in particular the location of the vortex core (X_Γ, Y_Γ), is shown in figure 3. The vortex core is clearly identifiable in the videos. The size of the core was of the order of millimetres and resulted in an error of the order $\pm 2\%$ in locating the 'centre' of the vortex. Experiments were repeated about ten times for each Reynolds number and the tank was allowed to settle for approximately 15 minutes.

3. Particle tracking

Quantitative information regarding the evolution of velocity and vorticity fields was obtained from a series of digital particle tracking experiments. The particle

tracking data provided instantaneous two-dimensional velocity fields from which information about the evolution of the vorticity field is generated. The experiments involved seeding the flow with 40 μm neutrally buoyant Kodak fluorescent microspheres, illuminating the piston cross-section as described above, and recording the vortex development. The videos were subsequently analysed to determine the path of particles through successive video frames and the velocity of the particles. The procedure for generating particle paths was to frame grab video images of the seeded flow field to 500×500, 8 bit (256 grey level) arrays and locating the centroids of the particles to sub-pixel accuracy. The intensity of a particle's image was assumed to be Gaussian and hence the sub-pixel centroid location was accomplished using a Gaussian curve fit, as outlined in Cowan & Monismith (1997). The next stage was to locate a particle identified in the first frame in three subsequent video frames. This involved first locating particles in the second frame in the neighbourhood of a particle in the first frame and making a prediction about where the particle will lie in the third frame. If a particle is successfully located in the third frame then a revised prediction was used to locate it in the fourth frame. Occasionally multiple tracks were identified. The track that was selected was the one that had a minimum variance of length and angle between successive video frames and also correlated with identified velocity vectors in the vicinity of the particle. Details of this process are described in Hassan & Cannaan (1993). If the length of the track is small, two further video frames were analysed to increase length of the track and hence reduce the error in the calculated velocity. For the experiments presented here the number of successful tracks identified in a single video frame is of the order 500. From this scattered non-regularized velocity information a global interpolation technique, similar to that outlined in Hardy (1971) and Spedding & Rignot (1993), was used to fit a surface to the experimental velocity data. Two surface functions were generated to describe the u and v components of velocity. These global functions were then used to generate information regarding the circulation and vorticity distribution of the developing vortex. Digital particle tracking was chosen for the current experiments due to the large dynamic range of velocities present in experiments. The accuracy of the particle tracking experiments was determined by

(i) the successful identification and tracking of the particles through successive video frames,

(ii) the type of algorithm that was used to interpolate the non-uniformly spaced velocity data to a regular grid, and

(iii) the ability of the particles to move with the local fluid velocity.

The error in locating and tracking the particle is a function of the size of its image, the seeding density and the local fluid velocity. The mean size of the particles in the video images was of the order 10 pixels. Gaussian fitting algorithms were used to locate the centroid of the particle to an accuracy of ± 0.25 pixels. This correlates spatially to an error in locating the centroid of the particles to ± 40 μm. The relative tracking error is then determined by the length of the track. In the regions of high velocity, i.e. in the separated vortex and in the boundary layer developing over the cylinder wall, the distance travelled by particles between video frames is of the order of 30 pixels and hence the relative velocity error is 2%. In regions of the flow distant from the separated vortex, where the particle is tracked through six video frames, the length of the path is often of the order 4 pixels and hence the relative velocity error is 10%.

Spedding & Rignot (1993) evaluated the performance of the global thin shell spline algorithm used in the current work and found the error to be relatively insensitive to

Symbol	D (mm)	$Re_{apparatus}$	A (mm s$^{-(m+1)}$)	m
□	170	3458	21.14	0.00
×	170	8936	53.98	0.02
■	138	3164	24.03	0.0
▷	170	8632	24.02	0.69
▽	170	10 213	45.15	0.335

TABLE 1. Velocity calibration results for the flow visualization experiments.

the grid spacing h and essentially a decaying function of L/δ, where L is the global length scale and δ is the mean distance between particles. Extrapolating these results to the current study with a local length scale of $L = 42$ mm and a mean particle spacing of $\delta = 2$ mm results in an estimation of the errors associated with the velocity and vorticity interpolating polynomial as being 2.5% and 5% respectively.

Chen & Emrich (1963) and Merzkirch (1987) described how to estimate the spatial resolution of a measurement based on the ability of particle to follow the flow. In the current experiment particles of 40 μm diameter were used. The density is 1.2 g cm^{-3} and the maximum fluid velocity is 6×10^{-2} m s^{-1}. This results in an estimate of the minimum spatial resolution due to the ability of the particles to track the fluid of the order 10 μm. Combining the different sources of error for the experiments described in this paper, using a 50×50 spline grid with $h/\delta \simeq 0.45$, results in an estimate of the error associated with the velocity and vorticity measurements, in the region of the separated vortex, the order of 5% and 8% respectively. In the low-speed sections of the flow the errors are the order of 12% and 18%.

4. Results

4.1. *Flow visualization results*

Table 1 gives velocity characteristics for the flow visualization experiments in the 170 and 138 mm diameter tubes. $Re_{apparatus}$, a Reynolds number based on cylinder wall speed At^m and piston diameter D, and defined as

$$Re_{apparatus} = D^{(1+2m)/(m+1)} A^{(1/(1+m))}/\nu,$$

is held constant throughout the duration of an experiment. If the wall speed is constant then $m = 0$ and $Re_{apparatus} = U_w D/\nu$ as defined in Hughes & Gerrard (1971).

The video sequences in figures 4(*a*) to 4(*e*) show the various stages of development of the vortex in front of the piston for the $Re_{apparatus}$ listed in table 1. The non-dimensional time t^* is defined as $t\nu/D^2$. The physical size of the images in figure 4(*a–d*) is 40×40 mm^2. Figure 4(*e*) shows the total cross-section of the toroidal vortex forming in front of the 138 mm diameter piston and provides an indication of the size of the vortex being measured in relation to the piston diameter. As noted in Pullin & Perry (1980) the best description of the centre of the vortex would come from the peak vorticity strength in the viscous sub-core. Comparisons between the centre of the spiral dye streakline and the streamline pattern generated from the particle tracking results (see figure 10 in § 4.2), indicate the path of the vortex core to be accurately marked with the fluorescent dye.

Figure 4(*a–e*) shows that the outer shape of the spirals is geometrically similar

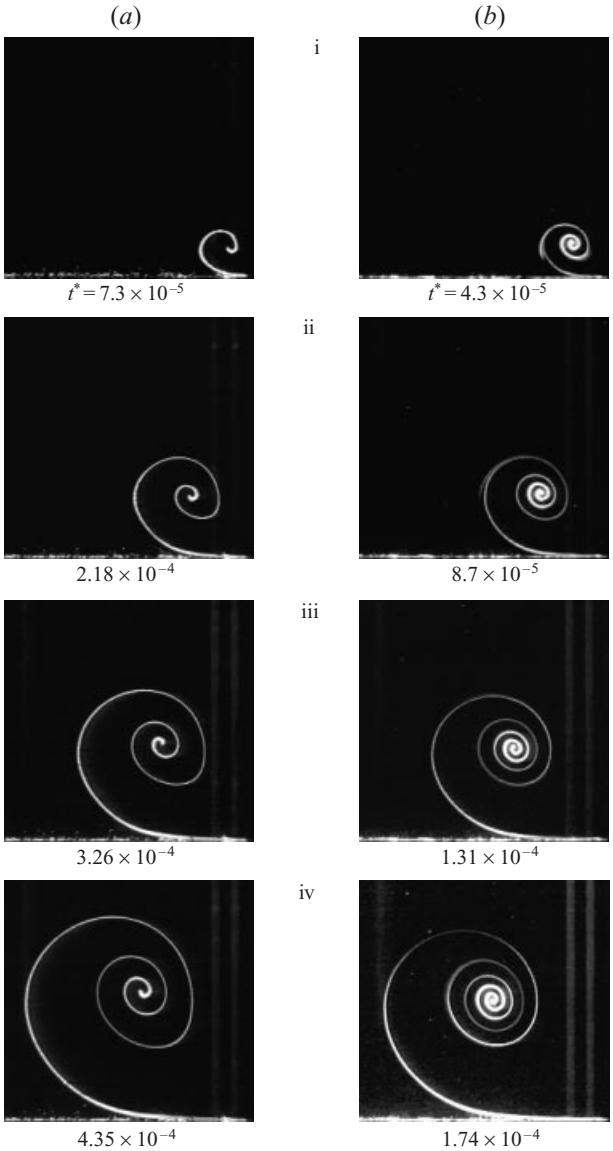

FIGURE 4 (*a, b*). For caption see page 9.

for the various $Re_{apparatus}$ considered and that the spirals also seem to scale in a self-similar fashion in time. It does appear however that the internal structure of the spirals is a function of $Re_{apparatus}$. The larger $Re_{apparatus}$ the more tightly wound the spiral appears for a given non-dimensional time. If we assume that the strength of the vortex core is increasing with $Re_{apparatus}$ and t^* then, in a qualitative sense, the number of spiral turns in the core is a function of the strength of the vorticity in the core. Figure 4(*a–e*) also shows that as m increases the number of turns on the spirals is reduced for equivalent $Re_{apparatus}$ and t^*. A similar effect was noted in the computations of Pullin (1978) for the structure of the vortex sheet formed at a wedge apex with a power-law starting flow. The computations showed that the vortex sheet was more loosely wound about the spiral centre as m increased and the proportion

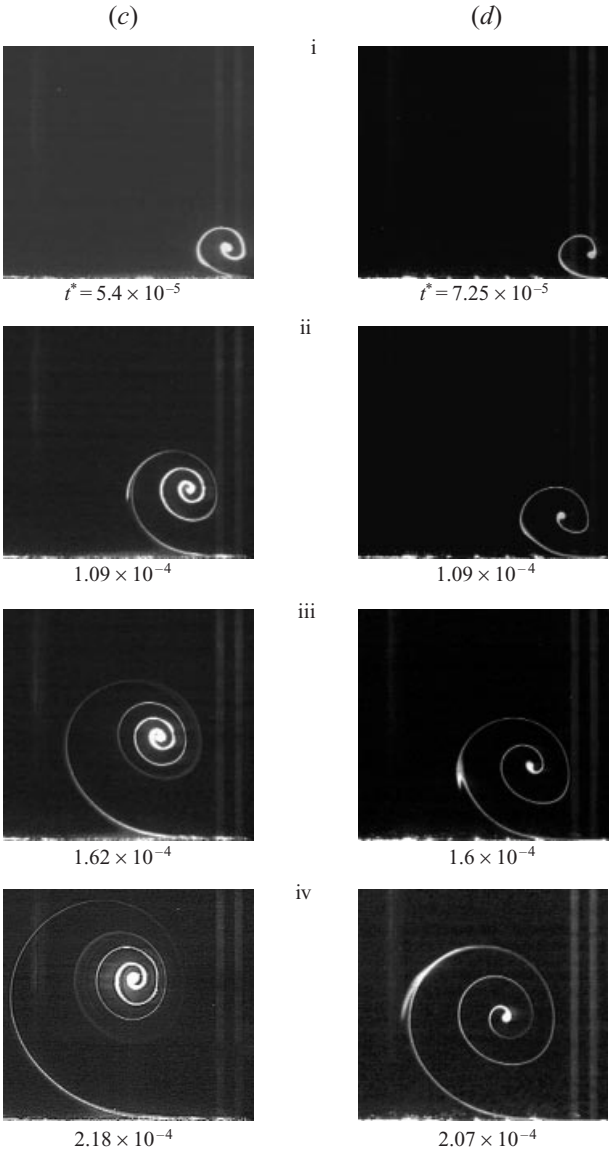

FIGURE 4. (*c, d*). For caption see facing page.

of the total circulation on the outer turns increased as m increased. The effect of reduced turns with increasing m indicates that the vorticity in the inner core becomes weaker as m increases. One can consider the impulsively started wall case, $m = 0$, as being the limiting case for the maximum inner core strength. As m increases the strength of the initial vorticity shed into the core decreases and results in a more loosely wound inner structure. The vortex cores universally display an elliptical shape with the semi-major axis having a slope of approximately 45° with respect to the piston face. It is not until the structure is of the same order in size as the apparatus length scale, see figure 4(*e*) at $t^* = 7.71 \times 10^{-4}$, that there is significant distortion of the structure from its earlier self-similar shape. One cause of this stretching is the self-induced effect of the vortex which has become more significant as the radius of

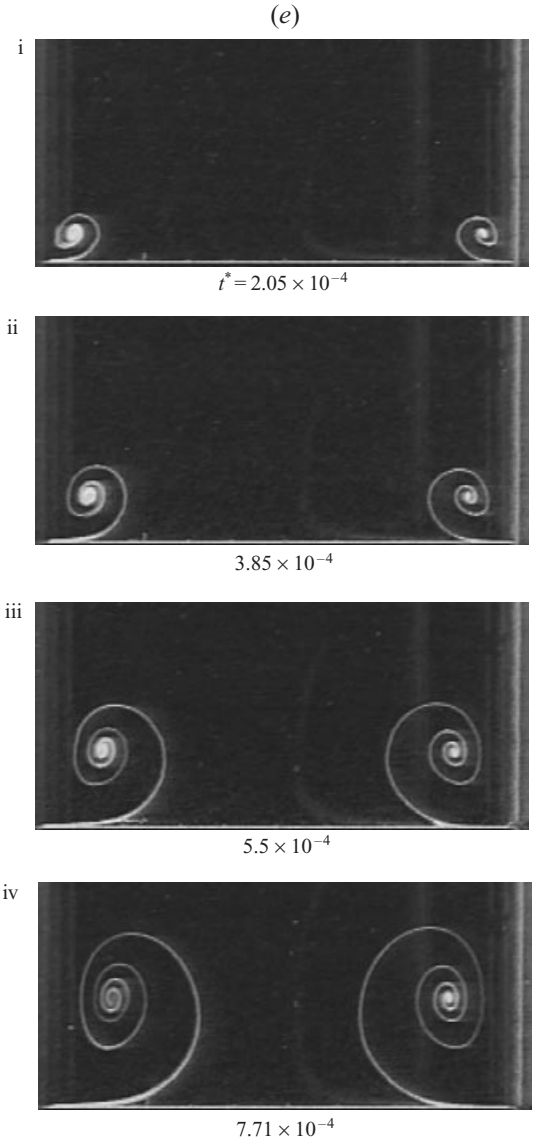

FIGURE 4. Video sequences for various $Re_{apparatus}$: (*a*) 3458, (*b*) 8936, (*c*) 10213, (*d*) 8632, (*e*) 3164.

the ring decreases and the strength of the vortex increases. The images also show that in all cases the location of the separation point of the boundary layer on the piston, as defined in figure 3, moves along the piston face and is located almost directly beneath the vortex core.

Figure 5 shows the trajectory of the vortex core for the cylinder wall velocity characteristics in table 1. The location of the vortex core is defined as (X_Γ, Y_Γ) as shown in figure 3.

In the early stages of vortex development the scaling of the vortex core coordinates are universal with respect to $Re_{apparatus}$ until X_Γ/D and $Y_\Gamma/D \simeq 0.1$. As the vortex develops beyond this point there is a trend for the trajectories to diverge and the rate of growth of the X_Γ-coordinate to slow relative to the rate of growth of the

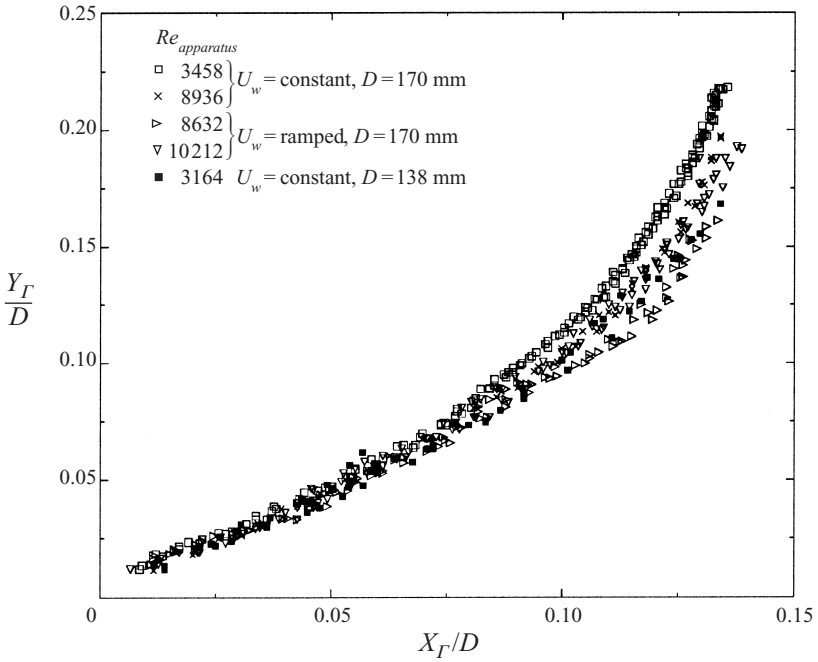

FIGURE 5. Plot of the trajectory of the vortex core for a range of $Re_{apparatus}$.

Y_Γ-coordinate. The scatter of the experimental results is relatively low, with an approximately $\pm 5\%$ spread around a mean result for a given $Re_{apparatus}$. Plots of X_Γ/D and Y_Γ/D versus t^*, figures 6(*a*) and 6(*b*) respectively, show that initially the core coordinates grow at an approximately constant rate. As the size of the vortex approaches the size of the experimental apparatus, $X_\Gamma/D, Y_\Gamma/D \simeq 0.1$, the growth rate of the X_Γ-coordinate slows appreciably while the Y_Γ-coordinate growth rate appears unaffected. For similar $Re_{apparatus}$ the growth rate of the X_Γ-coordinate is slower for the ramped velocity case ($Re_{apparatus} = 8632$) than the constant velocity case ($Re_{apparatus} = 8963$). The Y_Γ-coordinate also shows a similar trend with the ramped velocity data, being $\simeq 10\%$ smaller at the equivalent non-dimensional time. For $Re_{apparatus} = 8632$ when $t^* < 10^{-4}$ the data for the core location scales according to a strong power law; however, the growth rate does not continue to show the same power-law characteristic. Beyond $t^* > 10^{-4}$ for $Re_{apparatus} = 8632$ the growth appears linear.

If one assumes that the thickness of the boundary layer removed from the cylinder is similar in thickness to that forming over an impulsively started flat plate then an estimate of the 99% thickness of the boundary layer δ^* is $4\sqrt{\nu t}$. Figures 6(*a*) and 6(*b*) include plots of $\delta^*/D = 4\sqrt{\nu t/D^2}$ and show this length scale to be similar in size to the experimental measurements for the core when $t^* < 10^{-4}$ and 50% to 70% smaller than the core location when $t^* > 2 \times 10^{-4}$. Measurements of the distance between the cylinder wall and the inner turn of the dye spiral, $X_{entrain}$ in figure 7, indicates that $X_{entrain}$ is typically of the order of $X_\Gamma/2$. Comparison of $X_{entrain}$ with δ^* shows that the former is larger for most of the vortex development, implying that a narrow alleyway exists for entrainment of quiescent fluid into the vortex. This is illustrated in figure 7 and entrainment of fluid into the vortex can be seen occurring through the alleyway between the vortex core and the cylinder wall, see figure 3, and in the vorticity

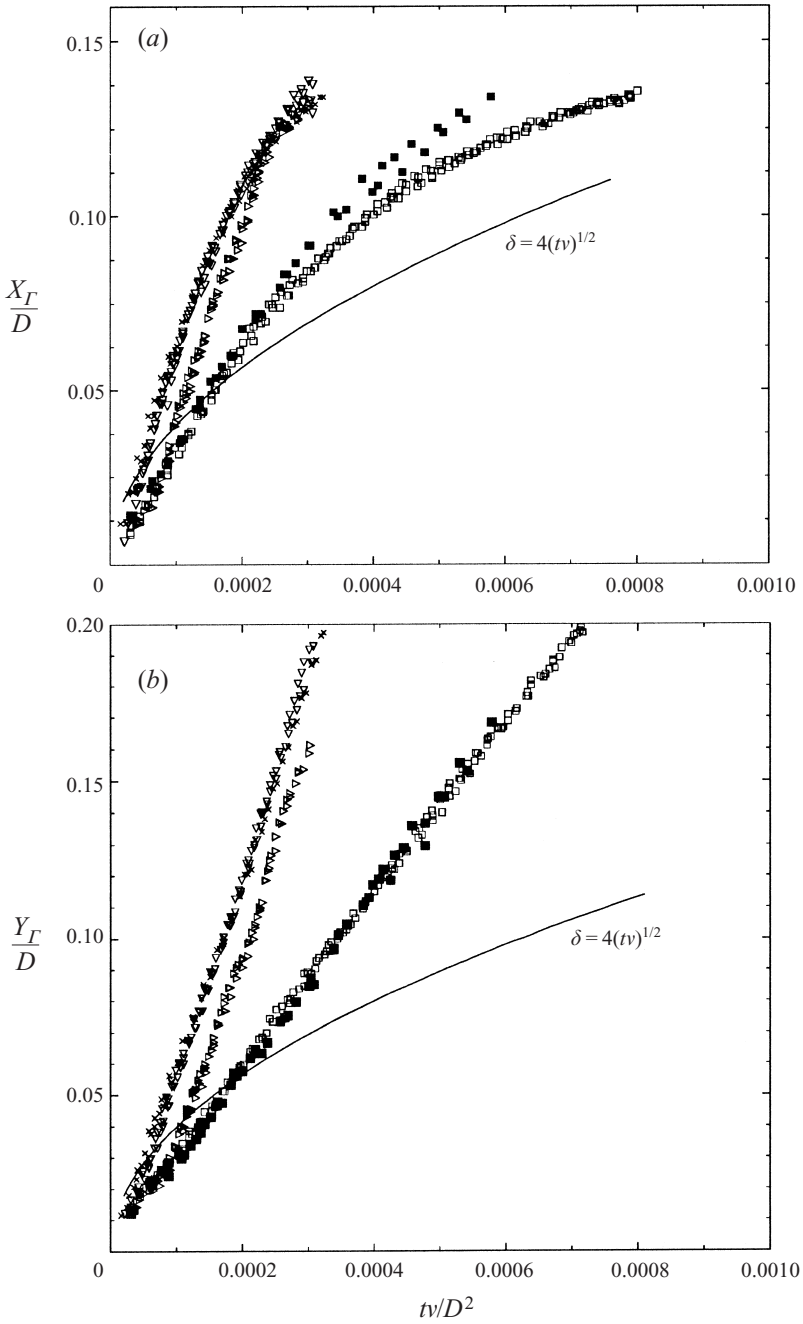

FIGURE 6. Plots of the variation of the location of the vortex core Z_Γ/D with respect to t^*. For symbols, see figure 5.

plots, figure 9(*b*), § 5.2. Measurements of the area of the vortex in Tabaczynski *et al.* (1970) and Allen (1997) suggest of the order of 60–90% the material in the vortex is from the separated boundary layer. As time increases the data shown in figures 6(*a*) and 6(*b*) display a stronger growth rate than $t^{1/2}$, indicating that the proportion of entrained inviscid fluid in the vortex increases with time.

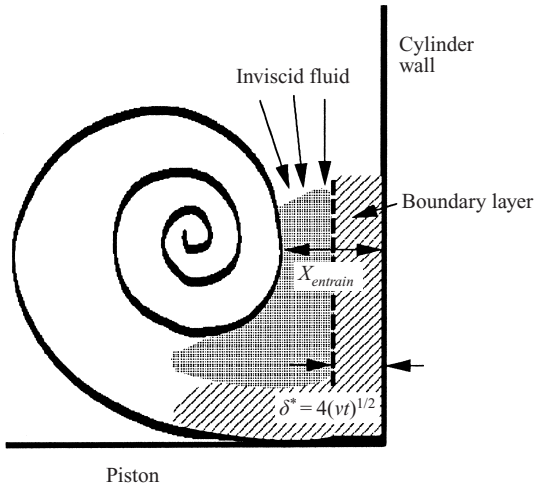

FIGURE 7. Entrainment alleyway of inviscid material into the vortex.

Symbol	D (mm)	$Re_{apparatus}$	A (mm s$^{-(m+1)}$)	m
□	170	3458	21.14	0.00
×	170	8936	53.98	0.02
▷	170	8632	24.02	0.69
◇	170	8601	42.3	0.20
○	170	7431	39.03	0.12

TABLE 2. Velocity calibration results for the particle tracking experiments.

4.2. *Particle tracking results*

Quantitative information regarding the velocity field of the vortex was obtained for the cylinder velocity characteristics listed in table 2. Figures 9(*a*) and 9(*b*) show streamline patterns and vorticity fields generated for $Re_{apparatus} = 8632$ and are representative of the results for Reynolds numbers in table 2. The size of the regions shown in figure 9 is 42 mm × 42 mm. The streamline patterns appear to grow spatially and temporally in a self-similar fashion about the vortex core. The vortex appears as a bubble, growing from the corner junction. The streamlines close to the piston face, under the vortex core, diverge away from the piston face. The vortex bubbles show a distinct tail that extends up the cylinder wall. The qualitative features of the integrated streamline patterns agree well with a time exposure photograph of particle traces shown in figure 8. The 'pinch-off' point of the tail of the vortex bubble is identified in figure 8.

The streamline patterns in figure 9(*a*) appear as spirals in the vortex core. This is thought to be a function of the errors involved with velocity measurements and the integration of the velocity field to generate streamlines. Streamline patterns in figure 9(*a*) show some indication of separation bubbles forming on the piston face. The local fluid velocity in this region is low relative to that in the vortex, resulting in a degree of uncertainty about the integrity of results for the streamline pattern on

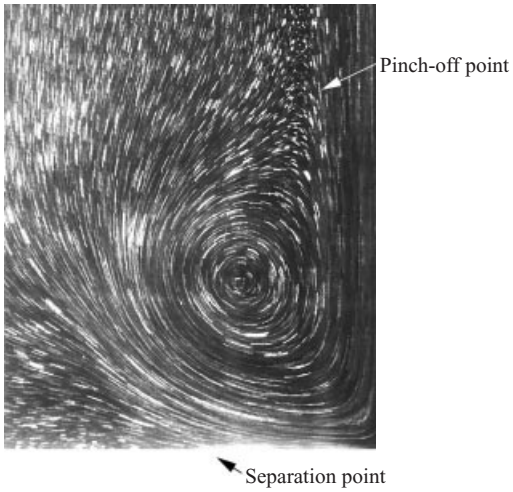

FIGURE 8. Particle pathline photograph for $Re_{apparatus} = 8632$, $t^* = 1.71 \times 10^{-4}$.

the piston face. Results of an axisymmetric enclosed cavity simulation of T. Mattner (1998, personal communication) indicate that a separation bubble forms on the piston surface in front of the developing vortex but the fluid velocities in the bubble are an order of magnitude smaller than that of the separated primary vortex.

Plots of the vorticity fields in figure 9(*b*) for $Re_{apparatus} = 8632$ show the shape, distribution and development of the vorticity field in front of the piston. The strength of the vorticity Ω was normalized with $D^{-2}v$. The vorticity is generated on the cylinder wall and is ejected into the cylinder from the corner junction, the separated vorticity forming an expanding, rotating and coherent spiral shape. Although somewhat diffuse, the shape of the vorticity distribution correlates well with the dye streakline. The outer turn of the vortex is clearly defined from the vorticity distribution but the vorticity in the inner core is diffuse and no inner spiral structure is evident. An alleyway where quiescent fluid is entrained can be seen between the cylinder wall and the vortex core. Figure 9(*b*) also shows a growing region of secondary vorticity wrapped around the outside of the primary structure. The secondary vorticity appears to grow at a rate similar to the amount of vorticity in the primary structure. The secondary vorticity is generated in order to preserve the no-slip condition on the piston face as the primary vorticity is being convected into the corner region. Figure 9(*b*) also shows fairly uniform development of the boundary layer on the cylinder wall. The vorticity profile in the boundary layer does not appear to be adversely affected by the vorticity being shed into the cylinder at the corner junction.

Figure 10(*a*) shows an image of the dye streakline overlaid on a corresponding vorticity field. The outer turn of the dye streakline clearly marks the boundary between the primary vorticity on the separated vortex and the induced secondary vorticity from the piston face. Figure 10(*b*) shows the streamline pattern overlaid on the vorticity field and illustrates that the focus from the streamline pattern is clearly located at the centre of the vorticity distribution of the primary vortex. The secondary vorticity has a plume-like distribution and is only indicated by a slight deviation in the streamlines.

Stokes theorem can be used to relate the contour integral of velocity $\boldsymbol{u}$ to the area

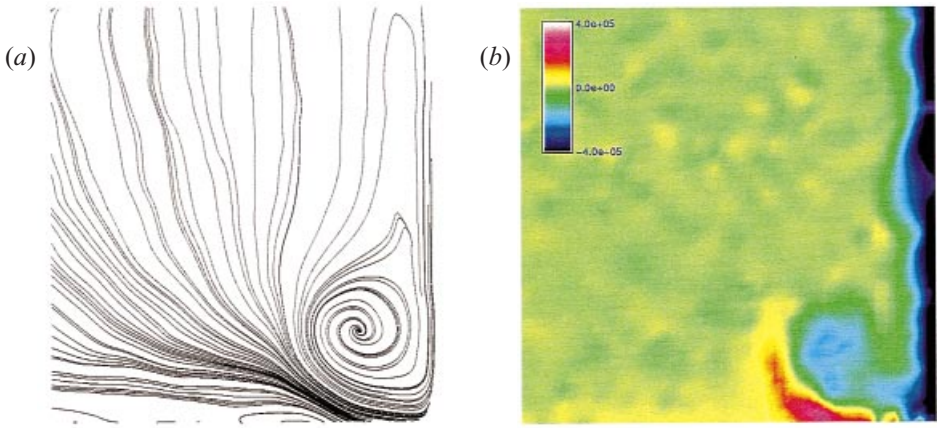

$t^* = 1.31 \times 10^{-4}$

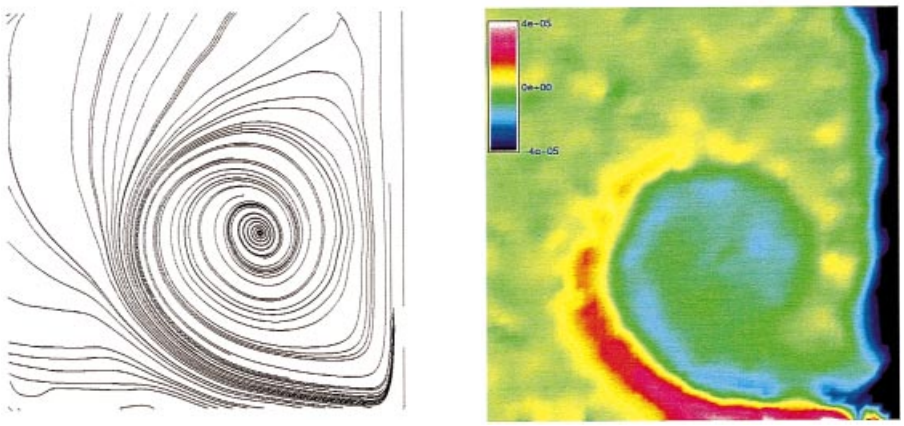

$t^* = 2.15 \times 10^{-4}$

FIGURE 9. Streamline patterns (*a*) and vorticity contours (*b*) for $Re_{apparatus} = 8632$, $m = 0.69$.

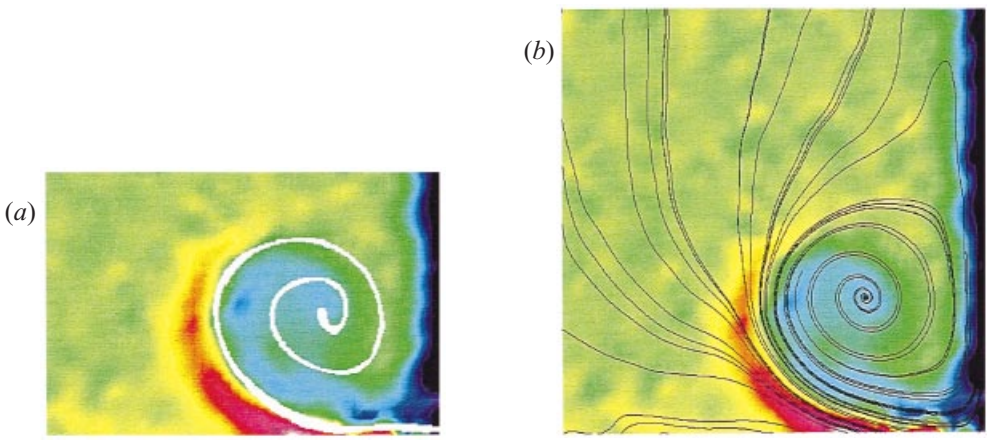

FIGURE 10. Comparison of vorticity field and dye streakline (*a*) and vorticity field and streamline pattern (*b*) for $Re_{apparatus} = 8632$, $t^* = 1.71 \times 10^{-4}$.

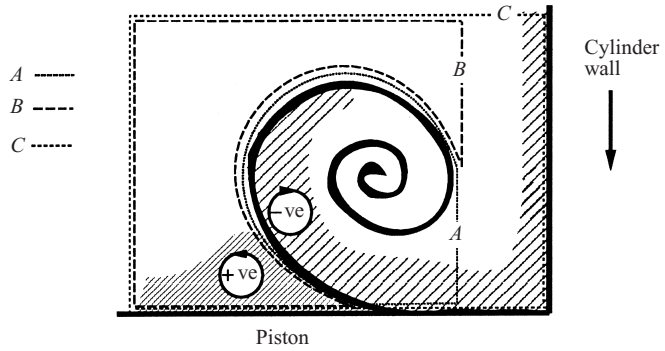

FIGURE 11. Diagram showing the presence of primary (−ve) and secondary (+ve) vorticity.

integral of the vorticity $\boldsymbol{\Omega}$ via

$$\Gamma = \oint \boldsymbol{u}\,\mathrm{d}\boldsymbol{s} = \iint \boldsymbol{\Omega}\,\mathrm{d}x\,\mathrm{d}y. \tag{4.1}$$

Figure 11 defines three different contours for which circulation data have been generated from the particle tracking velocity fields. Integration around contour A corresponds to the amount of vorticity ejected from the boundary layer into the inviscid fluid, Γ_A. Integration around contour B corresponds to the secondary vorticity on the piston face, Γ_B, formed in response to the primary vortex and hence of opposite sign to the vorticity in the boundary layer and primary vortex. The contour integral around C corresponds to the total vorticity within image area, Γ_C. The path of the contours of integration around the primary structure were evaluated from the zero-vorticity level (see figure 12). These contours corresponded well with the path marked by the outer turn of the dye spiral. There is a degree of uncertainty in completing contour A from the end of the zero-vorticity curve to the piston surface. However, this length was typically of the order of 10% of the total length of contour A and the flow in this region had only a small component of velocity tangent to the contour; hence contributions to the contour integral A were small and of the order of 2%. The path of contour B close to the cylinder wall is selected so as to not contain vorticity from the boundary layer on the cylinder wall.

The contour used for calculating Γ_A is shown in figure 12(b) and an example of the contour used for calculating Γ_B is shown in figure 12(c). Figures 13(a) to 13(c) show the results for the size of the circulation integrals, non-dimensionalized with v, plotted against t^* for the range of $Re_{apparatus}$ listed in table 2. Figures 13(a) and 13(b) show that the primary and secondary vorticity increase at approximately the same rate. The primary vorticity levels are only fractionally larger than the secondary vorticity levels. In order to test the sensitivity of the contour in calculating the vortex strength the integrals were repeated with a 5% variation of the contours. In all cases these integrations produced smaller results for Γ_A and Γ_B than those presented in figure 13(a, b), indicating that the method of finding the contour of zero vorticity level was successful. The results for the total circulation are shown compared with $\Gamma_w = 4.0 \times 10^4 \times U_w(t^*)$, indicated by the solid lines in figure 13(c). Γ_w represents the contribution to the circulation loop C from the cylinder wall. The small difference between the total circulation and the contribution from the cylinder wall indicates that the vorticity being shed at the corner junction is being matched closely by the generation of opposite-sign vorticity on the piston face.

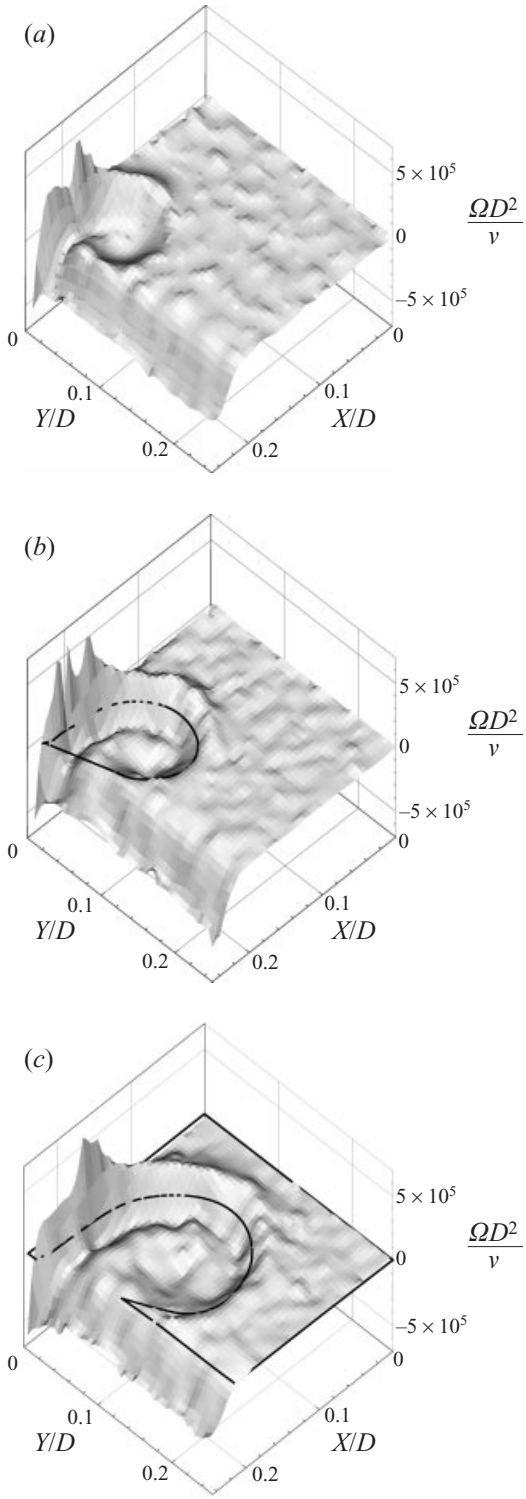

FIGURE 12. Vorticity fields with integration contours marked for $Re_{apparatus} = 7431$, $m = 0.12$: (*a*) $t^* = 1.26 \times 10^{-4}$, (*b*) $t^* = 1.5 \times 10^{-4}$, (*c*) $t^* = 2.16 \times 10^{-4}$.

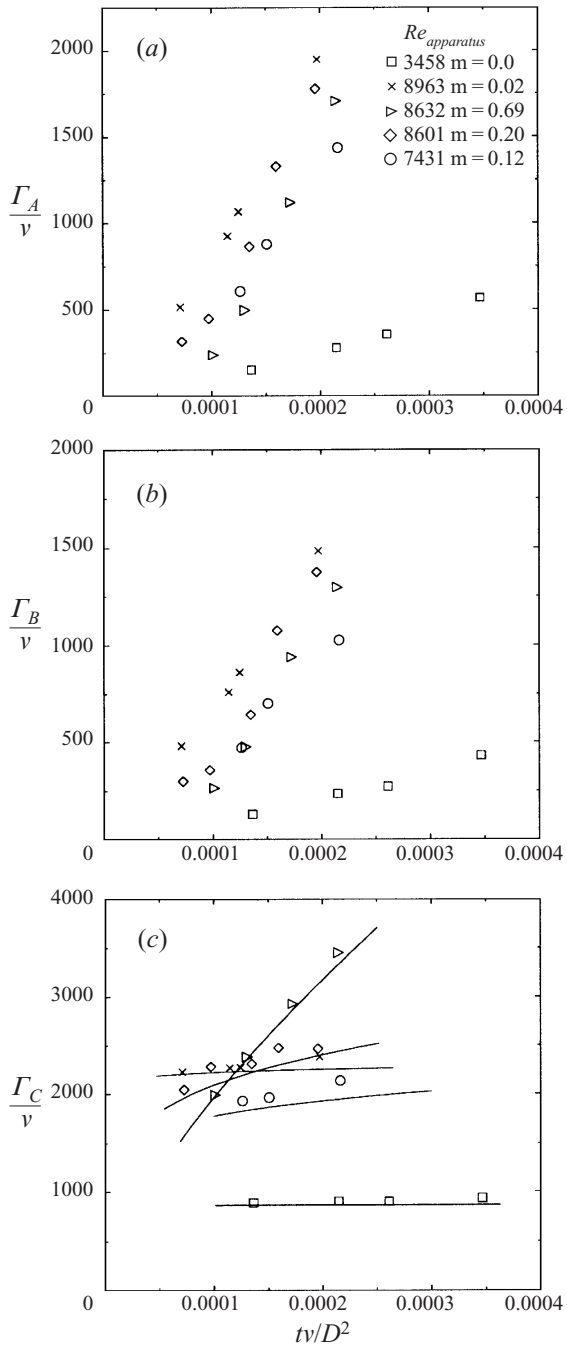

FIGURE 13. Results for circulation integrals around paths (*a*) *A*, (*b*) *B* and (*c*) *C*.

5. Discussion

5.1. *Introduction*

The problem of an inclined wall moving over another fixed wall, sometimes referred to as the scraping corner problem, was analysed by Taylor (1960) and Batchelor (1967).

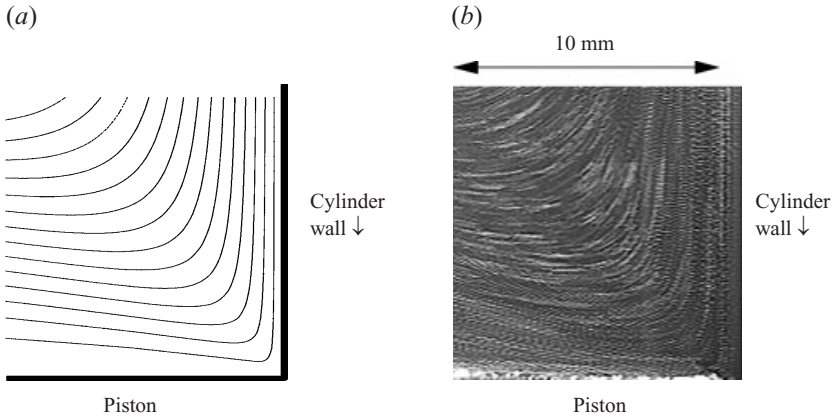

FIGURE 14. Self-similar streamline solution for flow close to the corner junction compared to an experimental pathline pattern for $Re_{apparatus} = 3458$, $t^* = 8 \times 10^{-4}$.

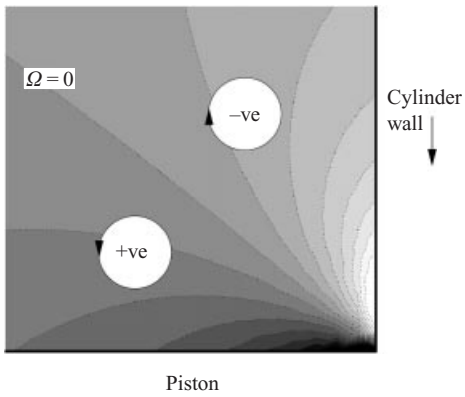

FIGURE 15. Analytic solution for the vorticity, $\Omega v/U_w$, in the corner region showing the corner singularity.

In the region of the corner the velocity gradients are large and a discontinuity exists in the velocity field at the junction of the moving piston and the fixed wall. In this region viscous forces are much larger than inertial ones. A steady viscous solution for the stream function ψ in the corner region can be generated from the steady Stokes equations $\nabla^2(\nabla^2\psi) = 0$. Figure 14(*a*) shows the calculated streamline pattern in the region of the corner junction from Taylor (1960). An order of magnitude argument from Batchelor (1967) implies that the distance r from the corner to where the steady viscous solution is applicable is of the order of $r \ll v/U_w$. Using water and a wall speed of 21.4 mm s^{-1}, corresponding to the minimum Reynolds number in this study, i.e. $Re_{apparatus} = 3458$, gives $r \ll 0.05$ mm. However, figure 14(*b*) shows a photograph of particle pathlines close to the corner junction from current experimental results. The scale of the photograph is orders of magnitude larger than the range over which the two-dimensional analytic solution is applicable. The similarity between the steady analytic streamline pattern and the instantaneous unsteady experimental pathline pattern indicate that the range of validity of the viscous solution is significantly larger than 0.05 mm. The experimental pathline photo clearly shows parallel flow close to the cylinder wall with pathlines diverging away from the piston face.

The corner flow solution predicts that the shear stresses on the piston become infinite at the corner. Taylor (1960) resolved this non-physical condition by arguing that the effect of this force is to lift the piston from the wall and relieve the corner stresses. The corner flow solution also indicates that an adverse pressure gradient exists on the piston face, in the direction moving away from the corner junction, resulting in a flux of vorticity into the flow of opposite sign that generated over the moving wall. Figure 15 shows a plot of contours of non-dimensional vorticity from the corner solution of Taylor (1960). The shape of the vorticity distribution is independent of the wall speed. The sign of the vorticity on the cylinder wall is opposite to that on the piston face, with the vorticity being singular in the corner. Figures 9(*b*) and 12 show similar rapid changes in the vorticity field close to the corner junction.

The flow inside an enclosed cavity with a moving wall is often used as a simple analogy for the more complicated family of separated flows past bluff bodies, e.g. Kim & Moin (1985). However, in these studies little consideration is given to the transient vortex formation in the moving corner.

Burggraf (1966) computed the steady location of the viscous vortex core in a cavity with one moving wall up to a Reynolds number, based on the width of the cavity and the wall speed, of 400. Although no transient behaviour was investigated, the vorticity distributions in the cell for this Reynolds number indicated a region of separated primary vorticity in the core and a region of opposite-signed secondary vorticity on the stationary cavity wall that has similar qualitative features to the vorticity distribution described in this paper. Burggraf (1966) stated that for Reynolds number greater than 100 there is a significant inviscid rotational core in the cavity.

A comparison between the inertial and viscous terms of the Navier–Stokes equations can be made from the experimental data for the velocity field. Evaluation of $\boldsymbol{u} \cdot \nabla \boldsymbol{u}$, $\nu \nabla^2 \boldsymbol{u}$ and estimations of $\partial \boldsymbol{u}/\partial t$ show that the inertial terms are an order of magnitude larger than the viscous terms in most of the flow field considered, including the region of the separated vortex. The exception is the immediate corner region where the viscous forces become large. The vortex is not a classical concentrated sheet of vorticity in an otherwise inviscid fluid, which is often used to describe the trailing vortex in the wake of an aircraft. However, the relative sizes of the inertial and viscous terms and the spiral shape in the vorticity distribution indicate that the separated vortex is an inviscid coherent structure.

Experiments show that separation of the vortex from the piston occurs almost instantaneously at the corner junction which suggests that the apparatus length scale is not a relevant variable to describe the early nature of the vortex roll-up. The viscous corner solution shows that an adverse pressure gradient develops on the piston face. This may be the reason for the separation of the boundary layer from the piston after it has negotiated the corner junction. A more physical explanation as to why the vortex moves away from the piston may be given in terms of the effects of secondary vorticity. Experimental studies, e.g. Walker *et al.* (1987), have shown that as a discrete vortex approaches a surface perpendicular to its direction of motion it induces the formation of secondary vorticity on the surface.

Numerical studies of Peace & Riley (1983), Tryggvason *et al.* (1990) and Ersoy & Walker (1985) examining vortex/surface interactions indicate that induced secondary vorticity causes the primary vortex to rebound from the surface. The secondary vorticity in these studies wraps itself around the outside of the rebounding vortex core, either as a discrete, separated element or as a continuous plume from the boundary layer on the surface. The results of Peace & Riley (1983) indicated that the

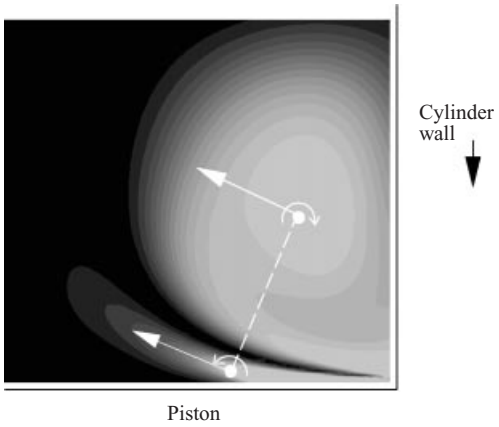

FIGURE 16. Illustration of the self-induced effects of secondary vorticy on the primary vortex.

wall region can act as a sink for the vorticity associated with the primary vortex. In these studies no apparatus length scale was involved. The relevant length scale is the distance between the two opposite-signed vortex cores.

In the current experiments, when the cylinder is set in motion a thin layer of highly concentrated vorticity is generated close to the cylinder surface which diffuses away from the wall and is convected into the corner junction. In order for the condition of no slip to be preserved on the piston face, secondary vorticity is generated continually at the piston face to match the primary vorticity being convected into the corner region. Experiments show that the secondary vorticity is wrapped around the primary structure in the form of a plume emanating from the piston face. The secondary vorticity induces the primary core to move away from the piston face and convect away from the corner. Figure 16 shows a diagram of the shape of the vorticity distribution in the corner region and how the opposite-signed distributions induce advection of the structure away from the corner.

5.2. *Experimental analysis*

The position of the vortex core and the vortex strength may be defined in terms of the following functional relationships: $Z_\Gamma = Z_\Gamma(A, t, \nu, D : m)$, $\Gamma_A = \Gamma_A(A, t, \nu, D : m)$ and $\Gamma_B = \Gamma_B(A, t, \nu, D : m)$ where Z_Γ represents the position of the vortex core $X_\Gamma + \mathrm{i}Y_\Gamma$. Γ_A is the amount of primary vorticity on the separated structure and Γ_B is the amount of induced secondary vorticity. Applying dimensional analysis these relationships can be expressed as

$$\frac{Z_\Gamma}{\sqrt{\nu t}} = \omega_\Gamma \left(\frac{A^2 t^{2m+1}}{(2m+1)\nu}, \frac{\sqrt{t\nu}}{D} \right), \tag{5.1}$$

$$\frac{\Gamma_A}{\nu} = \lambda_A \left(\frac{A^2 t^{2m+1}}{(2m+1)\nu}, \frac{\sqrt{t\nu}}{D} \right), \tag{5.2}$$

$$\frac{\Gamma_B}{\nu} = \lambda_B \left(\frac{A^2 t^{2m+1}}{(2m+1)\nu}, \frac{\sqrt{t\nu}}{D} \right). \tag{5.3}$$

If the amount of vorticity impinging on the piston in time t is estimated as $\frac{1}{2}\int_0^t U_w^2(\tau)\,\mathrm{d}\tau$ then the non-dimensional group $A^2 t^{2m+1}/((2m+1)\nu)$ is a Reynolds number, Re_Γ, proportional to the amount of circulation impinging on the corner junction. This is

the logical choice of Reynolds number, in preference to Re_{vortex}, as it has a physical meaning. If during the early stages of roll-up the apparatus length scale is not a relevant variable then the structure scales in a self-similar fashion and (5.1), (5.2) and (5.3) can be expressed as

$$Z_\Gamma/\sqrt{\nu t} = \omega_\Gamma(Re_\Gamma), \tag{5.4}$$

$$\Gamma_A/\nu = \lambda_A(Re_\Gamma), \tag{5.5}$$

$$\Gamma_B/\nu = \lambda_B(Re_\Gamma). \tag{5.6}$$

The study of self-similar vortical flows both experimentally and analytically has been extensive. A derivation of the similarity scaling for a semi-infinite vortex sheet in an otherwise inviscid flow field is contained in Saffman (1978), derived by considering the vortex roll-up to be independent of viscosity. As no external length scale was present, dimensional analysis was used to determine the scaling rate of the structure. In the current study there is no apparent external potential flow in which the vortex is embeddedd and as a result no obvious scaling law exists for the corner vortex at high Reynolds numbers. Departures from the non-dimensional self-similar scaling laws in the generation of vortex rings, e.g. Didden (1979), and rectilinear vortices, e.g. Auerbach (1987), have been attributed to a range of factors including the effect of an external length scale, the presence of secondary vorticity, finite Reynolds number effects and viscosity.

An alternative hypothesis evaluated with the present experimental data is that the vortex core trajectory is not affected by viscosity. If this were the case then the location of the core would be expected to be dependent on the apparatus length scale, wall speed and time, and if this were the case then the trajectory of the vortex core could be expressed non-dimensionally as $Z_\Gamma/D = \sigma_\Gamma(L_w/D)$.

5.3. *Flow visualization results*

Figures 17(*a*) and 17(*b*) show data sets for $X_\Gamma/\sqrt{\nu t}$ and $Y_\Gamma/\sqrt{\nu t}$ plotted against Re_Γ to test for a functional relationship between Z_Γ and Re_Γ. In general the data appear to scale universally for a period before diverging. The X_Γ data depart from the universal curve in a different fashion to the Y_Γ data. The X_Γ data show a peel-off and decline in growth rate as X_Γ approaches 25% of the size of the piston. There does not appear to be a significant difference between the ramped velocity cases and the constant velocity cases. The Y_Γ data appear to follow a fairly constant power-law growth throughout the experiment, after an initially flat section when $Re_\Gamma < 1000$. The curves for Y_Γ appear to be weakly offset as a function of m. The measurement error in calculating the non-dimensional groups $Z_\Gamma/\sqrt{\nu t}$ and Re_Γ is $\pm 2\%$.

Figure 17(*b*) shows that when the Y_Γ-coordinate is small the growth rate of the vortex appears to be slower than in the region of collapse when $Re_\Gamma > 1000$. In the early stages of vortex development it could be argued that the position of the vortex core is a function of viscosity and time alone and hence scales as $\sqrt{\nu t}$. There is weak agreement of this relation with experimental results for the Y_Γ-coordinate when $Re_\Gamma < 1000$. The X_Γ-coordinate does not show this trend at low Re_Γ. For $Re_\Gamma > 1000$ there appears to be a region of weak universal dependence of $Y_\Gamma/\sqrt{\nu t}$ and $X_\Gamma/\sqrt{\nu t}$ on Re_Γ. Curves of the form

$$Z_\Gamma/\sqrt{\nu t} = \omega_\Gamma \; Re_\Gamma^{q-1/2} \tag{5.7}$$

are shown fitted to the experimental data in figures 17(*a*) and 17(*b*); $\omega_\Gamma = \xi_\Gamma + \mathrm{i}\eta_\Gamma$ represents the non-dimensional core location. It can be seen that there is some

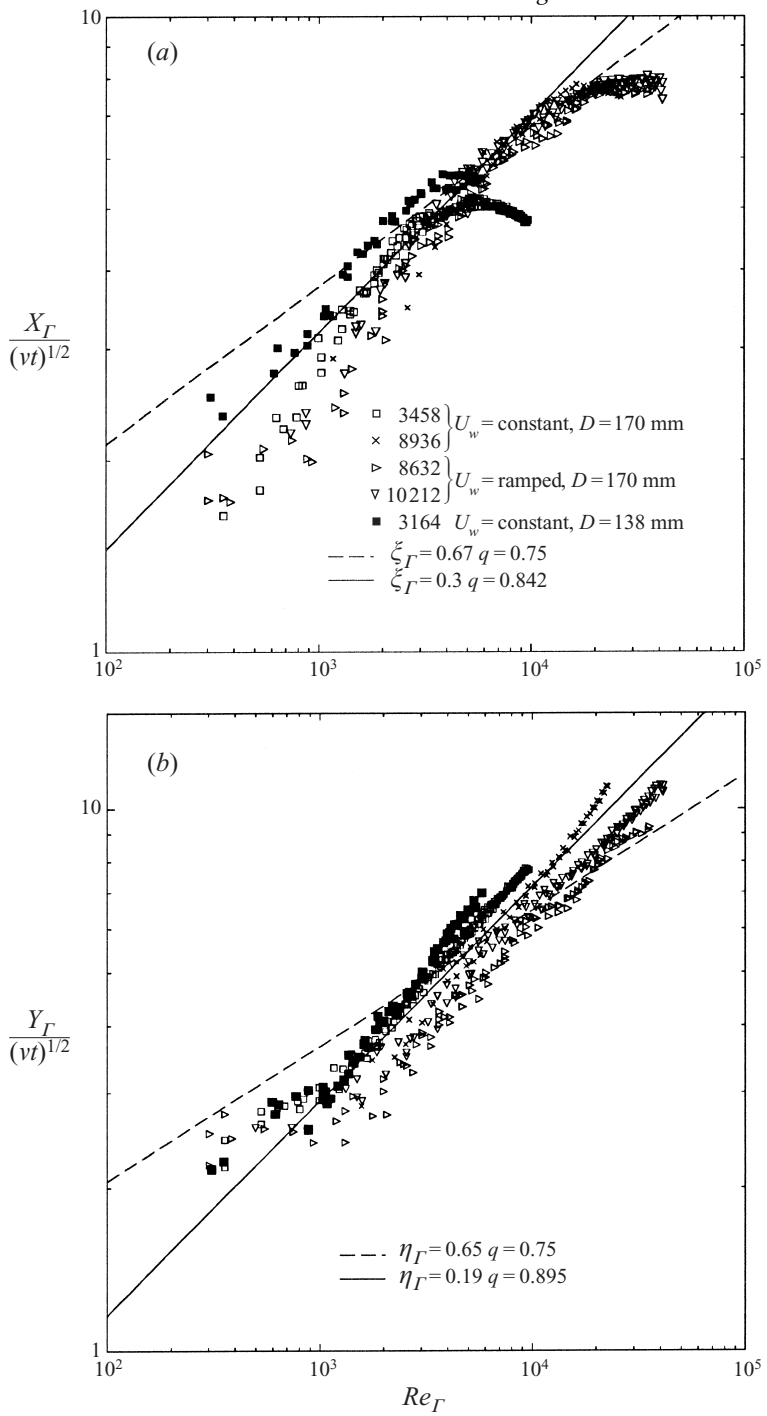

FIGURE 17. Plots of the variation of the location of the vortex core $Z_\Gamma/(vt)^{1/2}$ with respect to Re_Γ.

flexibility in fitting a curve to data with such a spread and this presents a difficulty in determining a scaling rate. In general the power laws of best fit for intermediate Reynolds numbers have $q \simeq 0.86$.

Power laws of the form $Re_\Gamma^{1/4}$ are also shown fitted to the experimental data in figure

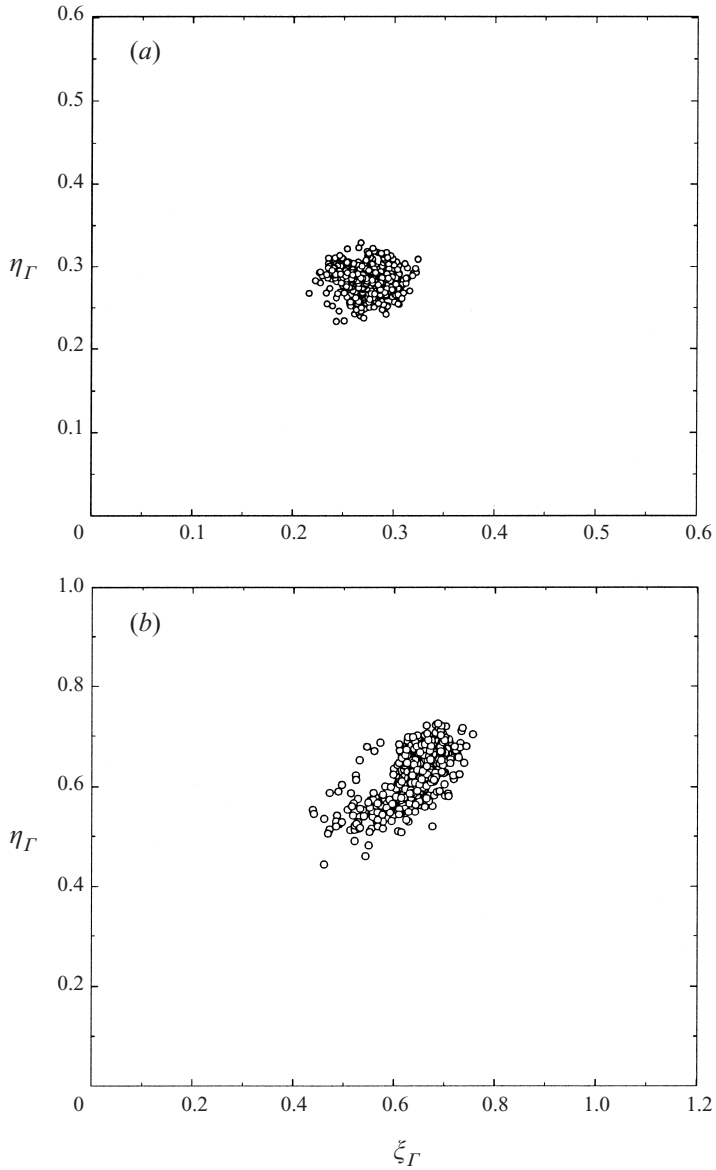

FIGURE 18. Plots of the location of the vortex core Z_Γ scaled with respect to (*a*) $t^{0.85}$ and (*b*) $t^{3/4}$.

17(*a*, *b*). This corresponds to the vortex structure scaling as $t^{m/2+3/4}$ and is the scaling predicted by a model where the distributed vortex is replaced by an isolated point vortex, as described in Allen (1997). This model indicates that the non-dimensional core location ω_Γ is a function of m. This scaling rate is the same as that predicted by Tabaczynski *et al.* (1970) derived from considerations of the area of the boundary layer detached from the cylinder wall. The difference between the power laws using $q = 0.85$ and $q = 3/4$ is significant. The models of Allen (1997) and Tabaczynski *et al.* (1970) do not take the effect of secondary vorticity on the piston face into account. The action of the secondary vorticity is to induce the primary structure to move away from the corner junction at a rate faster than $q = 3/4$. Figures 18(*a*) and

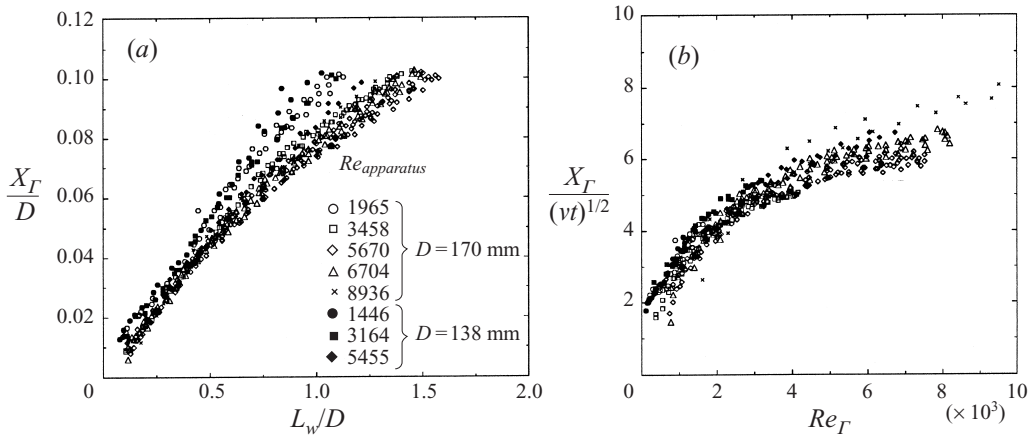

FIGURE 19. Plots of the X_Γ-coordinate of the vortex core forming in front of the piston.

18(b) show the location of the vortex core scaled with $Re_\Gamma^{0.35}$ and $Re_\Gamma^{1/4}$ respectively for the constant velocity data sets. This scaling corresponds to the core scaling as $t^{0.85}$ and $t^{3/4}$. The data shown are in the region where it appears that similarity applies, $Z_\Gamma/D < 0.1$ and $Z_\Gamma > 2\sqrt{\nu t}$. The collapse of data appears reasonable for both cases. However, the variation of data about the mean is an order of magnitude larger for the $t^{3/4}$ scaling than the $t^{0.85}$ scaling, which also can be inferred from the plots in figure 17(a, b). For $q = 0.85$ the mean non-dimensional core location is (0.275, 0.282) and for $q = 3/4$ it is (0.634, 0.65). Examination of the later stages of vortex development in figure 17(a) shows that $X_\Gamma/\sqrt{\nu t}$ diverges from the universal curve. The suggested reason for the slowing of the growth rate of the X_Γ-coordinate is that the external length scale, the piston diameter, is now affecting the trajectory of the vortex core and the vortex is experiencing a significant self-induced effect.

These plots show that the data sets for the different wall speeds peel-off from the universal curve at different Re_Γ. Generally, the larger $Re_{apparatus}$ is, the larger is the Re_Γ where the peel-off occurs. There appears to be an approximately linear relation between Re_Γ and $Re_{apparatus}$ for which peel-off occurs which can be expressed in the form $L_w/D \simeq 1.5$. In other words when the cylinder wall has moved $1.5 \times D$ the vortex is experiencing considerable self-induced effects.

In order to test the alternative hypothesis that Z_Γ scales as D and t we need to determine if Z_Γ/D is a function of L_w/D. From figure 19(a) it is evident that the X_Γ/D versus L_w/D data diverges. For $Re_{apparatus} = 1965$ and 8936, corresponding to the slowest and fastest wall speeds respectively, and at $X_\Gamma/D = 0.1$, figure 19(a) shows that the wall has moved about 50% further for the fastest wall speed. The spread of data in figure 19(a) does not appear to be function of the wall speed.

The spread data of data in figure 19(b) is of the order $\pm 7\%$ about the mean and this spread is fairly constant with respect to Re_Γ. These data do not show separation from the universal curve. This may be attributed to the fact that those selected are for $X_\Gamma/D < 0.1$ and hence our assertion that the structure should scale in a self-similar fashion while the size of the structure is an order of magnitude smaller than the apparatus length scale appears reasonable.

Figures 20(a) and 20(b) show plots of the experimental data for Z_Γ/D versus L_w/D for values of L_w/D up to 3. The plots show a continuing divergence of data as the

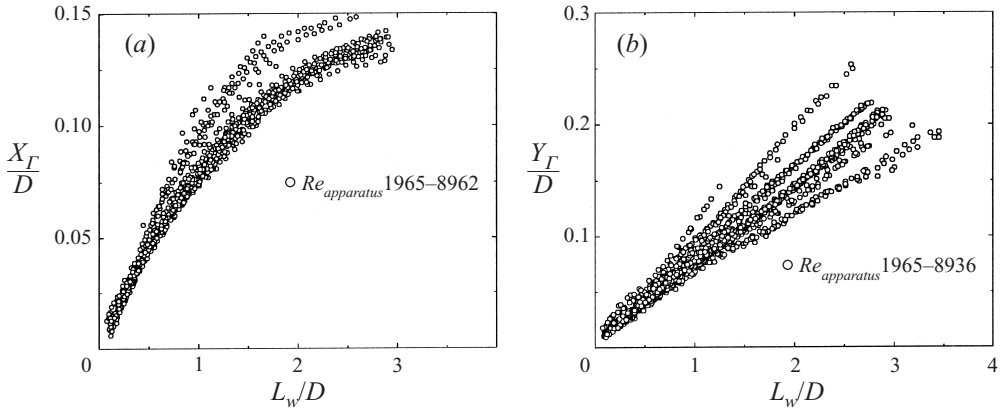

FIGURE 20. Combined plots of the location of the vortex core Z_Γ/D plotted against L_w/D.

vortex increases in size and there exists no region of uniform scaling of the form $Z_\Gamma/D = \sigma_\Gamma(L_w/D)$.

5.4. *Vortex strength results*

Figures 21(*a*) and 21(*b*) for $|\Gamma_A|/\nu$ and $|\Gamma_B|/\nu$ plotted with respect to Re_Γ show that the amount of primary and secondary vorticity scales universally as a linear function of Re_Γ. Curves of the form

$$\frac{|\Gamma_A|}{\nu} = 0.011\ Re_\Gamma \quad \text{and} \quad \frac{|\Gamma_B|}{\nu} = 0.088\ Re_\Gamma \tag{5.8}$$

are shown fitted to the data in figure 21(*a*, *b*). If the flux of vorticity from the corner junction into the fluid is approximated by the vorticity flux into the control volume through the boundary layer then

$$\frac{\mathrm{d}\Gamma_{slug}}{\mathrm{d}t} = \int_0^{\delta^*} \boldsymbol{\Omega} \cdot \boldsymbol{u}\ \mathrm{d}r \tag{5.9}$$

where $\mathrm{d}\Gamma_{slug}/\mathrm{d}t$ is the rate of increase of circulation of the vortex and δ^* is the 99% thickness of the boundary layer. Using $\Omega \simeq \partial u/\partial r$ (5.9) reduces to

$$\frac{\Gamma_{slug}}{\nu} = \tfrac{1}{2} Re_\Gamma. \tag{5.10}$$

This is often referred to as the 'slug' model from Maxworthy (1977) and commonly used to estimate the strength of a vortex ring formed by ejecting a slug of fluid from a cylinder in front of a piston moving with a velocity At^m. If we compare this to the experimental results for Γ_A it can be seen that, although the model predicts a linear scaling of the vortex strength, the total strength of the separated vortex is of the order of 25% of that predicted by the model. A possible cause for the difference between the model and the experimental results is the annihilation of primary and secondary vorticity. Taylor's corner flow solution suggests that the distance between regions of intense opposite-signed vorticity is small in the corner region and hence viscous diffusion could be acting a short distance away from the corner to diminish this vorticity flux.

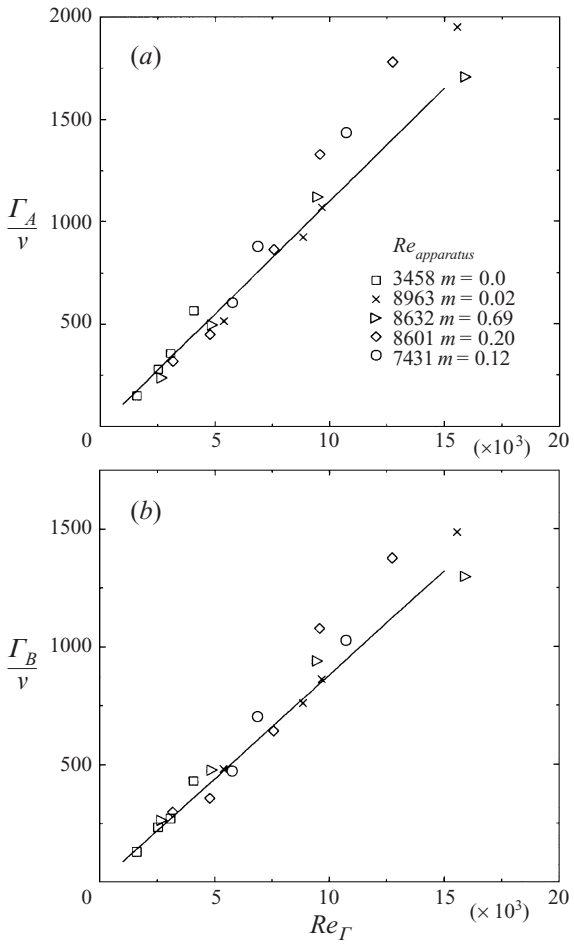

FIGURE 21. Primary Γ_A and secondary Γ_B vorticity development versus Re_Γ.

6. Conclusions

A set of experiments was undertaken to measure the trajectory of the vortex core and the strength of the vortex that formed in front of a circular piston for a range of velocity characteristics. As the size of the vortex increases it is suggested that a universal scaling law exists to describe the size and strength of the vortex that is independent of the apparatus length scale and dependent only on the wall velocity and viscosity. This scaling applies while the structure is still small with respect to external length scales and is expressed as

$$Z_\Gamma/\sqrt{\nu t} = \omega_\Gamma(m) Re_\Gamma^{0.35}, \quad |\Gamma_A|/\nu = 0.11 Re_\Gamma, \quad |\Gamma_B|/\nu = 0.088 Re_\Gamma. \tag{6.1}$$

The model of Allen (1997) and Tabaczynski *et al.* (1970) suggests that the size of the vortex should scale at the slower rate of $Re_\Gamma^{1/4}$ compared to $Re_\Gamma^{0.35}$. Apart from the fact that these scaling predictions have been developed from considerations of planar rather than cylindrical geometry, other reasons for the data not following the suggested scaling law are (i) the self-induced effects of the vortex ring and (ii) the effect of secondary vorticity production on the piston face. As the diameter of the ring decreases there is an enhanced self-induced velocity resulting in the rate

of growth in the axial direction being larger than predicted by similarity theory. This type of self-induced effect has been observed in experimental studies, e.g. Didden (1979), and in computations, e.g. Nitsche (1996). The secondary vorticity on the piston face will also have the effect of causing the structure to scale faster than predicted. This secondary vorticity causes the primary ring to separate and convect away from the piston surface. Measurements of the vorticity distribution in front of the piston indicate that the vortex is a coherent inviscid spiral structure for the range of $Re_{apparatus}$ considered. Viscous effects are limited to the immediate corner junction. The fact that secondary vorticity is generated which is similar in strength to the primary structure results in only a weak net increase in the circulation in the corner region, despite the continual convection of vorticity from the boundary layer on the cylinder wall. The circulation of the separated structure appears to scale linearly with respect to Re_Γ. This is the same as a model of the flow that equates the vorticity flux into the control volume with the increase of circulation on the separated eddy. However, the amount of vorticity on the separated vortex is $\simeq 25\%$ of that predicted by this 'slug' model and the suggested reason for the difference is that diffusion is acting in the immediate corner region to reduce the strength of the primary and secondary vortex.

This work was funded through the Australian Research Council and their support is gratefully acknowledged. The authors would like to thank Dr T. B. Nickels for writing the cross-correlation section of the particle tracking code.

REFERENCES

Allen, J. J. 1997 The formation of vortex sheets close to the junction of moving surfaces. PhD Thesies. University of Melbourne.

Auerbach, D. 1987 Experiments on the trajectory and circulation of the starting vortex. *J. Fluid Mech.* **183**, 185–198.

Batchelor, G. K. 1967 *An Introduction to Fluid Dynamics*. Cambridge University Press.

Burggraf, O. 1966 The structure of steady separated flows. *J. Fluid Mech.* **24**, 113–151.

Chen, J. & Emrich, R. 1963 Investigation of the shock-tube boundary layer by a tracer method. *Phys. Fluids* **6**, 1–9.

Cowan, E. & Monismith, S. 1997 A hybrid particle tracking velocimetry technique. *Exps. Fluids* **22**, 199–211.

Daneshyar, H., Fuller, D. E. & Deckker, B. E. L. 1973 Vortex motion induced by the piston of an internal combustion engine. *Intl J. Mech. Sci* **15**, 381–390.

Didden, N. 1979 On the formation of vortex rings: Rolling-up and production of circulation. *J. Appl. Math. Phys.* **30**, 101–116.

Ersoy, S. & Walker, J. 1985 Viscous flow induced by counter-rotating vortices. *Phys. Fluids* **28**, 2687–2698.

Hardy, R. 1971 Multiquadratic equations of topography and other irregular surfaces. *J. Geophys. Res.* **75**, 1905–1915.

Hassan, Y. & Cannaan, R. 1993 Full field bubbly flow velocity measurements using a multiframe particle tracking technique. *Exps. Fluids* **12**, 49–60.

Hughes, M. D. & Gerrard, J. H. 1971 The stability of unsteady axisymmetric incompressible pipe flow close to a piston. Part 2. Experimental investigation and comparison with computation. *J. Fluid Mech.* **50**, 645–655.

Ishikawa, N. & Daily, J. W. 1978 Observation of flow characteristics in a model I.C. engine cylinder. *SAE Paper* 780230.

Kim, J. & Moin, P. 1985 Application of a fraction step method to incompressible Navier–Stokes equations. *J. Comput. Phys.* **59**, 308–323.

Maxworthy, T. 1977 Some experimental studies of vortex rings. *J. Fluid Mech.* **81**, 469–495.

Merzkirch, W. 1987 *Flow Visualization*. Academic.

Namazian, S., Hansen, S., Lyford-Pike, E., Sanchez-Barsse, J., Heywood, J. & Rife, J. 1981

Schlieren visualization of the flow and density fields in the cylinder of a spark-ignition engine. *SAE Paper* 800044.

Nitsche, M. 1996 Scaling properties of vortex ring formation at a circular tube opening. *Phys. Fluids* **8**, 1848–1855.

Obokata, T. & Okajima, A. 1992 Roll-up vortex on the reciprocating piston in a cylinder. In *Proc. Sixth Intl Symp on Flow Visualization* (ed. Y. Tanida & H. Miyashiro), pp. 594–598. Springer.

Peace, A. J. & Riley, N. 1983 A viscous vortex pair in ground effect. *J. Fluid Mech.* **129**, 409–426.

Pullin, D. I. 1978 The large scale structure of unsteady self-similar rolled-up vortex sheets. *J. Fluid Mech.* **88**, 401–430.

Pullin, D. I. & Perry, A. E. 1980 Some flow visualization experiments on the starting vortex. *J. Fluid Mech.* **97**, 239–255.

Saffman, P. G. 1978 The number of waves on unstable vortex rings. *J. Fluid Mech.* **84**, 625–639.

Spedding, G. & Rignot, E. 1993 Performance analysis and application of grid interpolation techniques for fluid flows. *Exps. Fluids* **15**, 417–430.

Tabaczynski, R. J., Hoult, D. P. & Keck, J. C. 1970 High Reynolds number flow in a moving corner. *J. Fluid Mech.* **42**, 249–255.

Taylor, G. 1960 *Aeronautics and Aeromechanics*. Pergamon.

Tryggvason, G., Unverdi, S. & Song, M. & Abdollahi-Alibeik, J. 1990 Interaction of vortices with a free surface and density interfaces. In *Vortex Dynamics and Vortex Methods*. Lectures in Applied Mathematics, vol. 28 (ed. C. R. Anderson & C. Greengard), pp. 679–699. AMS.

Walker, J., Smith, C., Cerra, A. & Doligalski, T. 1987 The impact of a vortex ring on a wall. *J. Fluid Mech.* **181**, 99–140.